

Ortho-Para Chemistry of H₂CO in the Protoplanetary Disk TW Hya

M. Gaillard,[†] A. Faure,[†] P. Hily-Blant,[†] R. Le Gal,^{*,†,‡} S. Lee,[¶] H. Nomura,^{§,||} and
K. Furuya^{⊥,#}

[†]*Université Grenoble Alpes, CNRS, IPAG, F-38000 Grenoble, France*

[‡]*IRAM, 300 rue de la piscine, F-38406 Saint-Martin d'Hères, France*

[¶]*Korea Astronomy and Space Science Institute, 776 Daedeok-daero, Yuseong-gu, Daejeon
34055, Republic of Korea*

[§]*National Astronomical Observatory of Japan, 2-21-1 Osawa, Mitaka, Tokyo 181-8588,
Japan*

^{||}*Department of Astronomical Science, The Graduate University for Advanced Studies,
SOKENDAI, 2-21-1 Osawa, Mitaka, Tokyo, 181-8588, Japan*

[⊥]*RIKEN Pioneering Research Institute, 2-1 Hirosawa, Wako-shi, Saitama, 351-0198,
Japan*

[#]*Department of Astronomy, Graduate School of Science, The University of Tokyo, Tokyo,
113-0033, Japan*

E-mail: romane.le-gal@univ-grenoble-alpes.fr

Abstract

The spatial distribution of the chemical reservoirs in protoplanetary disks is key to elucidate the composition of planets, especially habitable ones. However, the partitioning of the main elements among the refractory and volatile phases is still elusive. Key parameters such as the carbon-to-oxygen (C/O) elemental ratio and the ionization fraction remain poorly constrained, with the latter potentially orders of magnitude lower than in the interstellar medium. Moreover, the thermal structure of the gas is also poorly known, despite its deep influence on gas-phase chemistry. In this context, ortho-to-para ratios could provide selective and sensitive probes. Recent ALMA observations have measured the spatially resolved column density of ortho- and para-H₂CO in the transition disk orbiting TW Hya and derived the radial profile of the ortho-to-para ratio. Yet, current disk models do not include the nuclear-spin-resolved chemistry required to interpret these observations. The present work aims to fill this gap, by combining a parametric disk physical model of TW Hya with the UGAN network, updated to include a comprehensive description of the nuclear-spin-resolved chemistry of formaldehyde. This new model successfully reproduces the observed column density of H₂CO to within a factor of 2, as well as the measured ortho-to-para ratio which varies from ~ 1.5 in the outer disk to ~ 3 inside 90 au. In particular the low value of this ratio beyond ~ 90 au is well explained by our model. However, the statistical value of 3 measured below ~ 70 au cannot be reproduced, suggesting that additional processes involving ices may be involved. Our parameter space exploration shows that the abundance of H₂CO is highly sensitive to the C/O elemental ratio and to the cosmic-ray ionization rate. Future observations of ortho- and para-H₂CO, based on well selected rotational transitions, in a large sample of disks, appear highly desirable.

Keywords: protoplanetary disks, formaldehyde H₂CO, ortho-para ratio, nuclear-spin chemistry, TW Hya

1 Introduction

Protoplanetary disks are the birthplaces of planetary systems, where complex physical and chemical processes govern the transformation of gas and dust into planets. A key challenge in disk studies is to establish how elements are partitioned between refractory material and volatile reservoirs (gas and ices), since this distribution sets the initial composition of forming planets, including potentially habitable ones. Despite major improvements in the observational (ALMA, JWST, NOEMA) and modeling capabilities, the spatial composition of protoplanetary disks remains only partially understood. In fact, an array of physical and chemical processes, acting on different time scales, makes a comprehensive self-consistent modeling of such environments a challenging task.^{1,2}

Among the most critical open questions are the two-dimensional temperature distribution, the spatial variations of the carbon-to-oxygen (C/O) budget, and the ionization fraction. Despite having a strong influence on molecular abundances, they are difficult to constrain observationally. To overcome these limitations, one approach is to focus on specific chemical tracers, such as isotopic ratios and nuclear-spin isomer ratios (so-called ortho-to-para ratios, OPRs).

Historically, OPRs have been used to infer the formation temperature of molecules in astrophysical environments.³ However, it is now clear that they rather reflect the current physical and chemical conditions in the gas.^{4,5} Still, OPRs are powerful tools because they are governed by spin-resolved branching ratios that obey rigorous nuclear-spin selection rules.⁶ Therefore, OPRs provide highly selective and accurate probes of physical and chemical conditions, especially temperature, ionization fraction, and chemical routes.^{5,7-9}

Formaldehyde (H_2CO) is a particularly valuable molecule in this context. It is both a common tracer in disks and a key intermediate in the chemistry leading to complex organic molecules. The nearby transition disk TW Hya, at a distance of only 59 pc, provides an ideal system in which to study the spin-chemistry of H_2CO . As one of the nearest and most extensively observed protoplanetary disks, TW Hya benefits from high-resolution ob-

servations that tightly constrain its physical and chemical structures. Its well-characterized temperature and density profiles, combined with a relatively low disk mass, make it an ideal testbed to benchmark disk chemistry models. While the first measurement of an H_2CO OPR in a protoplanetary disk was reported by Guzmán et al.¹⁰ toward HD 163296 using SMA and ALMA, more recent ALMA observations have spatially resolved the H_2CO OPR in the TW Hya disk.¹¹ These measurements open new means of investigating the physical and chemical conditions prevailing in protoplanetary disks, but interpreting them requires models that explicitly account for spin-resolved chemistry, a capability that existing disk models lack.

In this work, we address this gap by developing the first protoplanetary disk model that incorporates nuclear-spin chemistry for H_2CO . Using a parametric physical model of the TW Hya disk (presented in Section 2) in combination with the UGAN chemical network, extended to include a detailed description of formaldehyde spin chemistry (as described in Section 3), we investigate the radial abundance and column density distribution of ortho- and para- H_2CO and compare our predictions with ALMA measurements (see Section 4). Perspectives in the field of spin chemistry applied to disks are given in the last Section.

2 Methods

The chief objective of the present work is to compute the spatial distribution of the ortho- and para- H_2CO molecules in proto-planetary disks. To this aim, we have developed a steady-state parametric physical model for the density and temperature of the gas. Combined with the UGAN chemical network,⁹ this allows us to compute the abundance of both symmetries of H_2CO and compare them with observations in the TW Hya disk.

2.1 The Physical Disk Model

Our modeled disk has the commonly adopted azimuthal symmetry with a purely ortho-radial Keplerian velocity field, $v(r) = (GM_\star/r)^{1/2}$, with M_\star the mass of the central protostar, and r the radius.^{12–16} The disk is radially truncated between r_{in} and r_{out} . The radial profile of the mass density is dictated by the mass of the disk, M_{disk} , and by the radial profile of the surface density which assumes a power-law dependence, $\Sigma(r) = \Sigma_c(r/r_c)^{-\gamma_s}$, with Σ_c the value at the characteristic radius r_c , which is fixed by the normalization condition on the disk mass. The vertical mass density profile derives from balancing the pressure gradient and gravity, while adopting a perfect gas equation of state. Assuming that the vertical temperature gradient gives negligible contribution to the pressure gradient, the vertical density profile reduces to the hydrostatic one and a scale height is obtained, which depends only on the midplane temperature, $T_{\text{m,C}}$: $H(r) = H_c(r/r_c)^{\gamma_H}$ with $H_c \propto (T_{\text{m,C}}/M_\star)^{0.5}$. This assumption is justified by the fact that most of the mass is located close to the midplane. Finally, the mass density structure is given by $\rho(r, z) = (\Sigma(r)/H(r)/\sqrt{2\pi}) \exp(-z^2/2H^2(r))$ and is related to the number density of H nuclei $n_{\text{H}} = n(\text{H}) + 2n(\text{H}_2)$ through $\rho(r, z) = n_{\text{H}}(r, z)\mu_{\text{H}}m_{\text{a}}$ with m_{a} the atomic mass unit and $\mu_{\text{H}} = 1 + 4y$ where $y = n(\text{He})/n_{\text{H}} = 0.1$ is the present-day abundance of helium in the solar neighborhood. The number density of H nuclei is thus given by $n_{\text{H}}(r, z) = n_c(r/r_c)^{-\gamma_n} \exp[-z^2/2H^2(r)]$, where $n_c = \Sigma_c/(\sqrt{2\pi}H_c\mu_{\text{H}}m_{\text{a}})$ and $\gamma_n = \gamma_{\text{H}} + \gamma_s$. We have also considered another common analytical description of the surface density which includes an exponential taper at large radii:^{12,17} $\Sigma(r) = \Sigma_c(r/r_c)^{-\gamma_s} \exp[-(r/r_c)^{2-\gamma_s}]$.

Although the vertical temperature variations are neglected in deriving the density profile, they are not for the chemical calculations. The adopted vertical temperature profile models a continuous transition from a midplane temperature $T_{\text{m}}(r)$ to the atmospheric value in the upper layers of the disk, $T_{\text{a}}(r)$. In the present work, we adopt the following formulation,

$$T(r, z) = T_{\text{m}}(r) + \frac{T_{\text{a}}(r) - T_{\text{m}}(r)}{2} \left[1 + \tanh \left(\frac{z - z_0}{\Delta(r)} \right) \right]. \quad (1)$$

This is similar to a commonly used parametric profile,^{12,15,18} while consisting in a single function, with two parameters, z_0 and Δ , providing direct and independent control of the location and width of the transition from the midplane to atmospheric values. The hydrostatic assumption rests upon z_0/H being substantially larger than unity, and most models in the literature take $z_0/H \approx 3 - 4$. As is customary in parametric disk models, the midplane and atmospheric temperature profiles are radial power-laws, $T_m(r) = T_{m,C}(r/r_c)^{-\gamma_{T,m}}$ and $T_a(r) = T_{a,C}(r/r_c)^{-\gamma_{T,a}}$. The exponent $\gamma_{T,m}$ is related to the scale height exponent through $\gamma_H = (3 - \gamma_{T,m})/2$. The vertical temperature profile may, however, be much more complex than a single transition from a low to a high temperature. In fact, more physically based temperature distributions¹⁷ suggest that the gas temperature is better modeled with a two-layers profile. Therefore, we have considered a double-tanh temperature profile consisting of the sum of two profiles of the form given by Eq. (1) (see Model 3 in Table 2):

$$T(r, z) = T_m(r) + \frac{T_a(r) - T_m(r)}{2} \left[1 + \tanh \left(\frac{z - z_0}{\Delta(r)} \right) \right] + \frac{T'_a}{2} \left[1 + \tanh \left(\frac{z - z'_0}{\Delta'(r)} \right) \right], \quad (2)$$

where primed quantities refer to the upper layer. In what follows, we thus consider three models summarized in Table 1, and the free parameters are listed in Table 2. The parameters were obtained manually so as to reproduce the temperature profile of Andrews et al.¹² for Models 1 and 2, and of Lee et al.¹⁷ for Model 3.

The hydrostatic vertical density profile allows column densities to be computed with high accuracy using the error function, $\text{erfc}(z) = 2/\sqrt{\pi} \int_z^\infty e^{-t^2} dt = 1 - \text{erf}(z)$. We thus readily obtain the H nuclei column density above a given height z as:

$$N_H(r, z) = \sqrt{\frac{\pi}{2}} n_c H_c \left(\frac{r}{r_c} \right)^{-\gamma_S} \text{erfc} \left(\frac{z}{\sqrt{2}H(r)} \right). \quad (3)$$

In the above calculation, only one side of the disk is considered. The column density may then be converted in a visual extinction through²³ $N_H[\text{cm}^{-2}] = A_V \times 1.6 \times 10^{21}$.

The three physical models considered in this work have been constructed as follows. For

Table 1: Three Types of Models Considered in This Work (see also Table 2). For the gas-phase elemental abundances of carbon and oxygen (always given relative to H nuclei), a distinction is made above and below the CO snow surface. The gas-phase elemental abundance of nitrogen is fixed at half the ISM value, i.e. 3.2×10^{-5} , and the gas-phase elemental sulfur abundance is 8.0×10^{-8} .⁸ See Section 2.3 for details.

		Model 1	Model 2	Model 3
Temperature ^a		Single	Single	Double
Tapered density ^b		No	Yes	Yes
δ_C^c	above	30	30	30
	below	300	300	3000 ^d
δ_N^e		1.5	1.5	1.5
$[C/O]_{\text{elem}}^f$		1	1	1
		1	1	1
$[C/N]_{\text{elem}}^g$		6.5×10^{-2}	6.5×10^{-2}	6.5×10^{-2}
		6.5×10^{-3}	6.5×10^{-3}	6.5×10^{-4}

NOTES—^a Temperature profile using a single or double tanh as in Eq. (1). ^b Whether a tapered density profile is used or not. ^c Depletion factor $\delta_C = 8.3 \times 10^{-5}/[C]_{\text{elem}}$ above (first row) and below (second row) the snow surface. ^d A higher depletion is applied to reproduce the CO column density profile of Huang et al.¹⁹. ^e Depletion factor $\delta_N = 6.4 \times 10^{-5}/[N]_{\text{elem}}$. ^f The gas-phase elemental ratio above and below the snow surface. The elemental abundance of oxygen is computed as $[O]_{\text{elem}} = [C]_{\text{elem}}/[C/O]_{\text{elem}}$. ^g The elemental $[C/N]_{\text{elem}}$ ratio above and below the snow surface.

all models, the physical structure of Lee et al.¹⁷ (based on Kama et al.²²) was taken as a reference model. The power-law density profile in Model 1 is constrained by the disk mass between 4 and 200 au, and reproduces the reference density to within a factor of 2 from 10 to 165 au, and overestimates it by a factor of 4 at 200 au (see Fig. S1 in Supporting Information). Our midplane temperature power-law reproduces the reference values to better than 2 K between 10 and 150 au, and is 15 K lower at 200 au. The midplane temperature profile is common to all three models. The atmospheric temperature profile of Models 1 and 2 closely follows the parametric profile of Andrews et al.¹² In contrast, the two-layers temperature profile of Model 3 was fitted manually against the model of Lee et al.¹⁷, providing very good agreement up to $z/H \sim 3$ within 90 au, and up to $z/H \approx 2.5$ at larger radii (see Fig. S1 in Supporting Information). The 2D physical structures corresponding to models 1 to 3 are shown in Fig. 1.

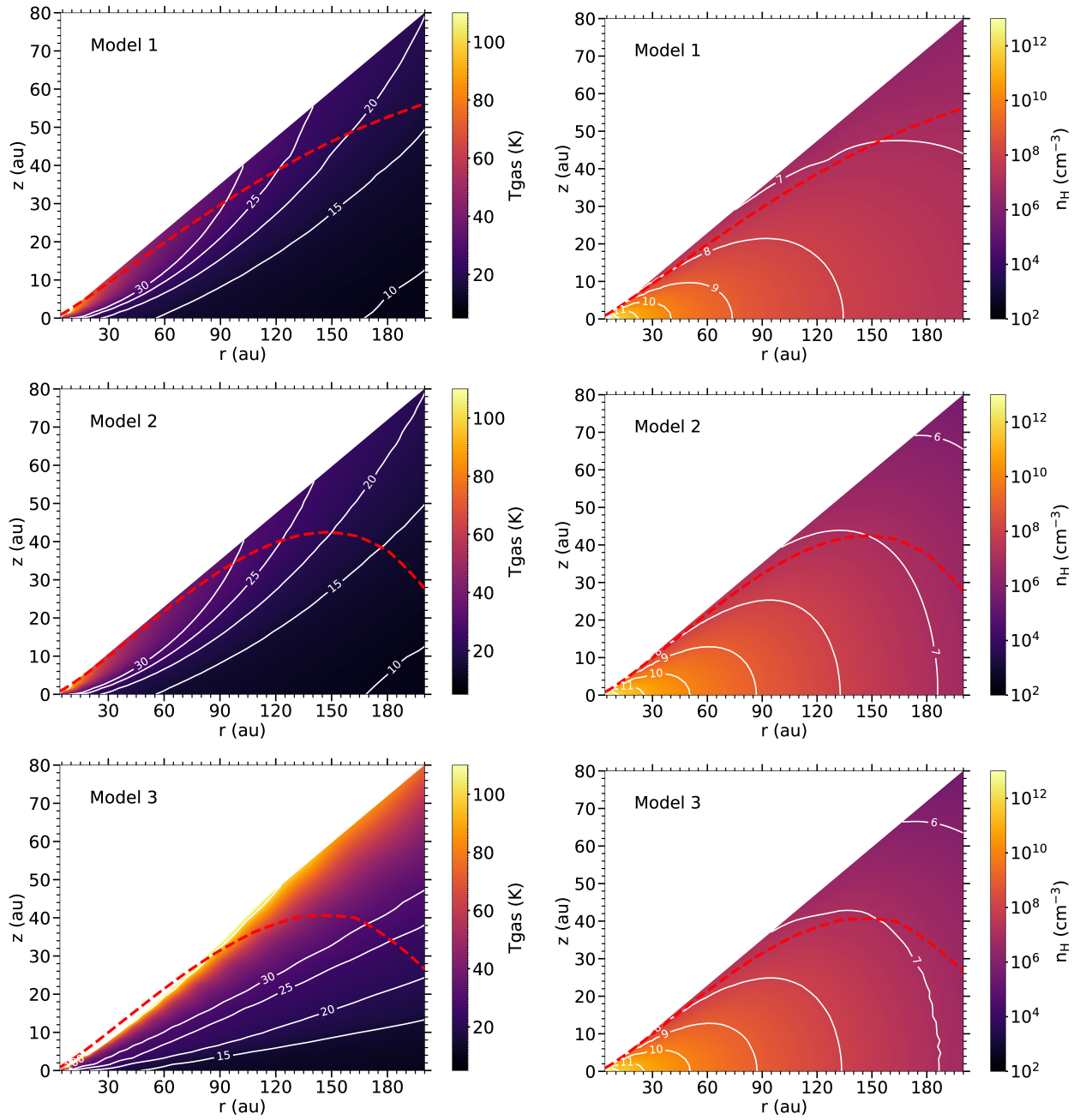


Figure 1: Disk physical structure from our three parametric models (Models 1 to 3 from top to bottom, see Tables 1 and 2). The 2D gas temperature (left) and total H density (right) are shown as colors, with iso-curves in white. The dashed red line corresponds to $A_V = 1$ mag (as measured from the top).

Table 2: Physical Parameters Used for Our Three Disk Models of TW Hya

Parameters	unit	Fiducial	Model 1	Model 2	Model 3 ^a
M_\star	M_\odot	0.8 ^b			
M_{disk}	M_\odot	0.023 ^c			
y		0.1 ^d			
r_{in}	au	4			
r_{out}	au	200			
r_c	au	35			
H_c	au		3.5	3.5	3.5
γ_{H}			1.325	1.325	1.3 ^e
Σ_c	g cm^{-2}		5.2	11.0	11.0
γ_{S}			2.5	1.0	1.0
n_c	10^{10} cm^{-3}		1.7	3.6	3.6
T_{m}	K		$16(r/r_c)^{-0.35}$	$16(r/r_c)^{-0.35}$	$16(r/r_c)^{-0.35}$
T_{a}	K		$54(r/r_c)^{-0.5}$	$54(r/r_c)^{-0.5}$	$25(r/r_c)^{-0.3}$
T'_{a}					400
z_0	au		1.5	1.5	0.4
z'_0	au				3.5
$\Delta(r)$	au		1.0	1.0	0.2
$\Delta'(r)$	au				$(r/r_c)^{0.15}$

NOTES—^a For the temperature in Model 3, the expressions for T_{m} , T_{a} , z_0 , and $\Delta(r)$ refer to the lower and primed quantities are for the upper layer. ^b From Cantá et al.²⁰, Qi et al.²¹. ^c From Kama et al.²². ^d $y = n(\text{He})/n_{\text{H}}$. ^e Exponent taken from Lee et al.¹⁷.

2.2 Ortho-Para Chemistry of Formaldehyde in UGAN

The UGAN nuclear-spin-resolved chemical network was originally developed from the work of Flower et al.²⁴ (hereafter F06) devoted to the chemistry of prestellar cores. It includes species containing H, D, He, C, N, O, S and separates the nuclear-spin states of H_2 , H_2^+ , H_3^+ (including deuterated isotopologues) and those of carbon, nitrogen, oxygen and sulfur hydrides. A first update of F06 consisted in a revision of the nitrogen hydrides chemistry was presented in Le Gal et al.⁸ The nuclear-spin selection rules were derived using the method of Oka,²⁵ which is based on the conservation of the rotational symmetry of the nuclear-spin isomers. The second update by Hily-Blant et al.⁹ (hereafter HB18) consisted of extending the work of Le Gal et al.⁸ to the entire F06 network in a systematic manner for all hydrides containing C, N,

O, and S atoms, along with their deuterated forms for N- and O-hydrides. The nuclear-spin selection rules were derived from the permutation symmetry approach of Quack,²⁶ which is more general than the method of Oka²⁵ and adapted to deuterium nuclei. The selection rules depend on the reaction mechanism, with two limiting cases: hopping (direct exchange) and full scrambling (indirect exchange) of protons. In HB18 and in this work, full scrambling is assumed because at low temperatures (i.e. below ~ 100 K), reactions generally proceed via long-lived intermediate complexes where complete randomization of identical nuclei takes place. Direct evidence of nuclear-spin selection rules in a reaction involving a long-lived complex was in fact observed only recently using ultracold experimental techniques.²⁷ On the other hand, we note that ion-trap measurements on the deuterated isotopic variants of the $\text{HCl}^+ + \text{H}_2 \longrightarrow \text{H}_2\text{Cl}^+ + \text{H}$ reaction indicate that this reaction proceeds via proton-hop, with no evidence of scrambling,²⁸ in agreement with classical trajectory calculations.²⁹ It should be noted that the proton-hop scenario would result in statistical nuclear-spin ratios, i.e. an OPR of 3 for H_2CO , as predicted for the deuterated isotopologues of ammonia.³⁰ The third update by Faure et al.⁵ consisted of a revision of the oxygen hydrides chemistry, and particularly that of water. Subsequent targeted updates to the UGAN network were published in Hily-Blant et al.^{31, 32} Many reaction rate coefficients were also updated from a literature survey.

We describe below the fourth major update of UGAN, which primarily involves a revision of the carbon hydrides chemistry and the introduction of the ortho-para chemistry of formaldehyde. Specifically, we have:

- added H_2CO , HCO , H_2CO^+ and H_2COH^+ as new gas-phase reactive species.
- updated the nuclear-spin-resolved chemistry of CH_3 and $\text{O}(^3P)$, the key precursors of H_2CO .
- implemented revised branching ratio for CH_5^+ dissociative recombination based on CRYRING storage-ring experiments.³³

- incorporated low-temperature neutral-neutral destruction pathways of H₂CO with CN and C₂H, constrained by recent CRESU (Cinétique en Écoulement Supersonique Uniforme) measurements.^{34,35}
- adopted new dissociative recombination rates for H₂COH⁺,³⁶ with branching ratios consistent with observational constraints.³⁷

2.2.1 Formation Pathways

The chemistry of H₂CO can follow three distinct routes: (i) ion-neutral gas-phase chemistry, (ii) neutral-neutral gas-phase chemistry and (iii) surface chemistry. The first route should proceed via the radiative association of HCO⁺ with H₂ or H, followed by dissociative recombination or charge exchange, but this route is unlikely to be dominant.³⁸ The primary neutral-neutral formation pathway in the gas-phase should be the reaction between the radical CH₃ and atomic oxygen O(³P),



Finally, efficient formation of H₂CO by the hydrogenation of CO in H₂O–CO ice was demonstrated experimentally at 10 K using an atomic hydrogen beam experiment.³⁹ The second and third routes should therefore compete in cold (hereafter ‘cold’ refers to kinetic temperatures below 100 K) environments, but the variations of their relative importance with varying physical conditions has yet to be established. In particular, the ice route requires an efficient thermal or nonthermal desorption mechanism for releasing intact H₂CO into the gas-phase. Despite experimental efforts, such a mechanism has so far remained elusive.⁴⁰

In this work, the second and third routes are considered, with surface chemistry being treated only implicitly by assuming that the grains have a static ice mantle composed of H₂O, CO, CO₂, H₂CO, etc. (their abundances relative to H₂O can be derived from Table 3 of HB18) with a canonical H₂CO abundance of 6% with respect to water ice.⁴¹ Thus, there are

ices everywhere in the molecular layer but adsorption and depletion are not treated explicitly: the abundances of solid species (relative to H nuclei) are set by the depletion factors that vary above and below the snow surface (see Section 2.3), while their relative abundance with respect to solid water (from HB18) remain fixed. As a result, the ice and gas phases are treated as separate reservoirs, and the OPR and abundance of gaseous formaldehyde results exclusively from gas-phase reactions. The major updates of **UGAN** thus concern the nuclear-spin-resolved chemistry (formation and destruction) of CH_3 , $\text{O}(^3P)$, and H_2CO . We also note that the OPR of H_2CO in ice should equal the statistical value of 3, as supported by theory and laboratory experiments (see Yocum et al.⁴², and references therein).

Carbon hydrides chemistry in cold environments starts with the slow radiative association:



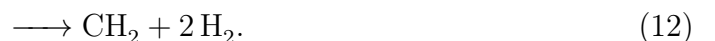
followed by an exothermic and fast hydrogen abstraction leading to the pivotal CH_3^+ ion:



and, finally, another slow radiative association with H_2 :



forming the radical CH_3 , among other products, after dissociative recombination:



The above set of reactions should dominate the formation of CH_3 in cold environments. An important update of UGAN concerns reactions (8)-(12) where the thermal rate coefficient and branching ratios were taken from the CRYRING storage-ring measurements of Kamińska et al.³³ We note that a key reaction regarding the ortho-para chemistry of CH_3 (and thus H_2CO) is the nuclear-spin thermalization¹ of CH_3^+ by H_2 , which will set the OPR of CH_5^+ and then CH_3 (see Supporting Information). Such thermalization processes are typically neglected in the UGAN network, except the fast equilibration reactions of H_2 with H^+ , H_3^+ and HCO^+ (and their deuterated variants). However, efficient proton scrambling should occur in the protonated methane (CH_5^+)* complex, as supported by the fast isotopic H-D exchanges observed in the reaction $\text{CH}_3^+ + \text{HD} \longrightarrow \text{CH}_2\text{D}^+ + \text{H}_2$ (see Gerlich⁴³ and references therein). Thermalization by H_2 should thus drive the OPR of CH_3^+ toward thermal equilibrium above a critical temperature of $\sim 15 - 20 \text{ K}$ ⁷, where $\text{OPR}(\text{CH}_3^+)$ should converge toward the statistical value of 1. The thermalization reaction of CH_3^+ by H_2 was added in our network following the state-to-state statistical approach of Rist et al.⁶

Oxygen atoms react primarily with H^+ to create O^+ ions (by charge transfer) or with H_3^+ to form OH^+ and H_2O^+ :



The above reaction was revisited recently using merged-beam measurements by Hillenbrand et al.⁴⁴ Thermal rate coefficients for the two product channels were derived by these authors for the temperature range from 10 to 1000 K, and a temperature-dependent branching ratio was observed. We adopted the thermal rate coefficients where the fine-structure level populations of $\text{O}(^3P_J)$ are assumed in thermal equilibrium (see Table 2 of Hillenbrand et al.⁴⁴).

Finally, as explained above, formaldehyde should predominantly form via the reaction of

¹Thermalization here refers to CH_3^+ reaching a nuclear-spin equilibrium via proton scrambling, which is not necessarily full thermal equilibrium.

CH₃ with atomic oxygen (reaction (4)), for which a competing channel is



The most recent kinetic measurements for the CH₃+O reaction report a total rate coefficient of $\sim 1-2 \times 10^{-10} \text{ cm}^3 \text{ s}^{-1}$ over the temperature range 259–2580 K, being $1.26 \times 10^{-10} \text{ cm}^3 \text{ s}^{-1}$ at room temperature, and with a temperature-independent branching ratio of 55% for H₂CO + H and 45% for CO + H₂ + H,⁴⁵ in very good agreement with the calculations of Xu et al.⁴⁶ We adopted the rate coefficient and branching ratio of Hack et al.⁴⁵ with no temperature dependence. We note, however, that measurements below 100 K would be highly beneficial.

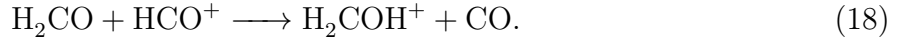
2.2.2 Destruction Pathways

Destruction of formaldehyde is dominated by reactions with the abundant CN and C₂H radicals and with HCO⁺. The rate coefficients for the destruction of H₂CO by C₂H and CN were measured recently down to 22 K using the CRESU technique.^{34,35}

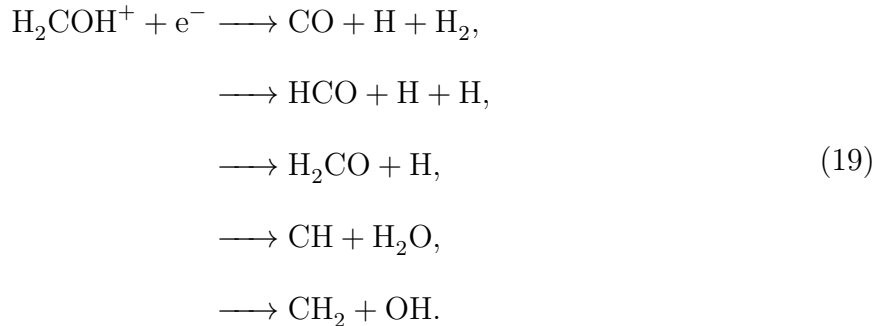


These reactions belong to a class of neutral-neutral processes that accelerate below ~ 200 K, where the temperature dependence changes from positive to negative. The postulated mechanism involves the formation of a weakly bound van der Waals complex, whose lifetime is prolonged at low temperature, and tunneling through a small activation barrier.⁴⁷ This is indeed supported by *ab initio* calculations which can be fitted to the experimental data to provide rate coefficients over a large temperature range. The recommended best-fit expressions from West et al.³⁴ and Douglas et al.³⁵ for reactions with CN and C₂H, respec-

tively, were adopted in UGAN. Another key destruction pathway of H_2CO is the protonation reaction with HCO^+ :



For this reaction, and other similar ion-molecule reactions involving H_2CO or HCO , we used the capture theory of Su & Chesnavich⁴⁸ for ion-polar molecule collisions. We note, in particular, that the formaldehyde cation H_2CO^+ can form via the charge transfer reaction $\text{H}_2\text{CO} + \text{H}^+ \longrightarrow \text{H}_2\text{CO}^+ + \text{H}$ and via the protonation of HCO by e.g. HCO^+ . While there is no measurement for the dissociative recombination (DR) of H_2CO^+ (we use the KIDA⁴⁹ recommendation), the DR of H_2COH^+ was measured at the CRYRING storage-ring by: Hamberg et al.³⁶



The rate coefficient and partial branching ratios were taken from, Hamberg et al.³⁶ with the additional assumption that the channels preserving the C-O bond (experimental branching ratio of 92%) are distributed among CO (31%), HCO (30%) and H_2CO (31%). The branching ratio for the HCO channel (30%) is the upper limit derived by Bacmann et al.³⁷ from the HCO and H_2COH^+ column densities measured in the prestellar core L1689B.

The rate coefficients for the updated and new reactions in UGAN are listed in Table 3 in the form of Arrhenius-Kooij fits.

2.3 Elemental Gas-Phase Abundances

The partitioning of the main elements (carbon, nitrogen, oxygen, sulfur) among the solid (refractory grains) and volatile (gas, ice) phases is a central, yet still elusive, question in

Table 3: Summary of Key Updated and New Reaction Rate Coefficients Adopted in the UGAN Network

Reactants	Products	α [$\text{cm}^3 \text{s}^{-1}$]	β	γ [K]	Reference	Comment
$\text{CH}_5^+ + \text{e}^-$	$\rightarrow \text{CH}_4 + \text{H}$	5.34(−08)	−0.72	0	(1)	Update
	$\rightarrow \text{CH}_3 + \text{H}_2$	5.23(−08)	−0.72	0	(1)	Update
	$\rightarrow \text{CH}_3 + \text{H} + \text{H}$	7.61(−07)	−0.72	0	(1)	Update
	$\rightarrow \text{CH}_2 + \text{H}_2 + \text{H}$	1.88(−07)	−0.72	0	(1)	Update
	$\rightarrow \text{CH} + 2 \text{H}_2$	3.60(−08)	−0.72	0	(1)	Update
$\text{O} + \text{H}_3^+$	$\rightarrow \text{OH}^+ + \text{H}_2$	4.65(−10)	−0.14	0.67	(2)	Update
	$\rightarrow \text{H}_2\text{O}^+ + \text{H}$	2.08(−10)	−0.40	4.86	(2)	Update
$\text{CH}_3 + \text{O}$	$\rightarrow \text{H}_2\text{CO} + \text{H}$	6.94(−11)	0	0	(3)	New
	$\rightarrow \text{CO} + \text{H}_2 + \text{H}$	5.68(−11)	0	0	(3)	New
$\text{H}_2\text{CO} + \text{CN}$	$\rightarrow \text{HCN} + \text{HCO}$	3.72(−12)	−1.09	5.2	(4)	New
$\text{H}_2\text{CO} + \text{C}_2\text{H}$	$\rightarrow \text{C}_2\text{H}_2 + \text{HCO}$	2.38(−11)	−0.41	−3.0	(5)	New
	$\rightarrow \text{C}_2\text{H}_2 + \text{CO} + \text{H}$	2.51(−11)	−0.37	−3.54	(5)	New
$\text{H}_2\text{CO} + \text{HCO}^+$	$\rightarrow \text{H}_2\text{COH}^+ + \text{CO}$	2.87(−09)	−0.46	0	This work	New
$\text{H}_2\text{COH}^+ + \text{e}^-$	$\rightarrow \text{CO} + \text{H} + \text{H}_2$	2.39(−07)	−0.78	0	(6)	New
	$\rightarrow \text{HCO} + \text{H} + \text{H}$	2.31(−07)	−0.78	0	(6)	New
	$\rightarrow \text{H}_2\text{CO} + \text{H}$	2.39(−07)	−0.78	0	(6)	New
	$\rightarrow \text{CH} + \text{H}_2\text{O}$	1.54(−08)	−0.78	0	(6)	New
	$\rightarrow \text{CH}_2 + \text{OH}$	4.62(−08)	−0.78	0	(6)	New

NOTES—The rate coefficients are of the form $k(T) = \alpha (T/300)^\beta \exp(-\gamma/T)$. Fits are reliable over the kinetic temperature range $T = 10 - 100$ K. Numbers in parentheses are powers of ten. References: (1) Kamińska et al. ³³; (2) Hillenbrand et al. ⁴⁴; (3) Hack et al. ⁴⁵; (4) West et al. ³⁴; (5) Douglas et al. ³⁵; (6) Hamberg et al. ³⁶

disk chemical modeling.^{2,17} Moreover, the relative amount of volatile carbon and oxygen, the $[\text{C}/\text{O}]_{\text{elem}}$ ratio, is known to have a dramatic impact on the chemical abundances.^{8,50} In the context of the present work, the $[\text{C}/\text{O}]_{\text{elem}}$ ratio is anticipated to play an important role in H_2CO chemistry. Because CO is the main reservoir of carbon, photodissociation of CO, as well as adsorption to and desorption from ices, are essential processes for disk chemistry. The photodissociation front defines the upper limit of the molecular layer, above which CO is efficiently destroyed by UV photons, as in Photon Dominated Regions (PDRs). In this work, the photodissociation front is defined as the region where the visual extinction (increasing downward, see Eq. (3)) is equal to 1 mag.⁵¹ The molecular layer extends down to the snow surface, defined as the $T = 25$ K iso-temperature surface,^{12,19,51} below which CO is primarily in ices on grains. The intersection of the snow surface with the disk midplane is the CO snow-

line, such that CO is entirely released in the gas phase at smaller radii. In the present work, photodissociation is not included, and the impact of gas-grain exchanges is taken into account through depletion factors applied to the ISM gas-phase fractional elemental abundances, as is customary in disk modeling.^{12,15,17,19,50,52} The ISM values are taken from Table 2 of HB18, except for sulfur (see our Table 1). Thus, a depletion factor $\delta_C = 8.3 \times 10^{-5}/[C]_{\text{elem}}$ is used for the gas-phase elemental carbon abundance $[C]_{\text{elem}}$. Distinct depletion factors characterize the gas phase in the molecular layer and below the snow surface. The oxygen elemental abundance is then determined from the value of $[C/O]_{\text{elem}}$ as $[O]_{\text{elem}} = [C]_{\text{elem}}/[C/O]_{\text{elem}}$. Although it is expected that the $[C/O]_{\text{elem}}$ should vary spatially, a uniform value $[C/O]_{\text{elem}}=1$ is adopted in all the present models.^{17,52} Similarly, a depletion factor $\delta_N = 6.4 \times 10^{-5}/[N]_{\text{elem}}$ is employed for the nitrogen gas-phase elemental abundance, but with no distinction above and below the CO snow surface. Finally, the initial abundances for the gas-phase species in each cell of the disk are not atomic but molecular. They are precalculated using an initially atomic gas with depleted elemental abundances as given in Table 1, under physical conditions corresponding to two cells at the outer edge of the disk, respectively above and below the CO snow surface (in practice with $T_{\text{gas}} \sim 10 - 30$ K and $n_{\text{H}} \sim 10^7 \text{ cm}^{-3}$, see Fig. 1).

The carbon depletion factors (above and below the snow surface) were constrained by the CO column density measured in TW Hya.¹⁹ The results are shown in Fig. 2. The difference between Models 1 and 2 is due to the exponential tapering of the density profile in the outer disk. It was also found that the vertical temperature profile in Model 3 requires typically ten times larger a depletion below the snow surface in order to reproduce the observed CO column density. In contrast to carbon and oxygen, observational constraints on the nitrogen elemental abundances (or C/N ratios) in disks are very limited due to the lack of dipole-allowed rotational lines of N_2 , the presumably main nitrogen reservoir.⁵² The nitrogen depletion factor is therefore difficult to quantify, but it could be (loosely) constrained here thanks to the impact of $[N]_{\text{elem}}$ on the H_2CO column density, as discussed below. The adopted values of δ_C and δ_N are summarized in Table 1. We note that the corresponding N/O ratios

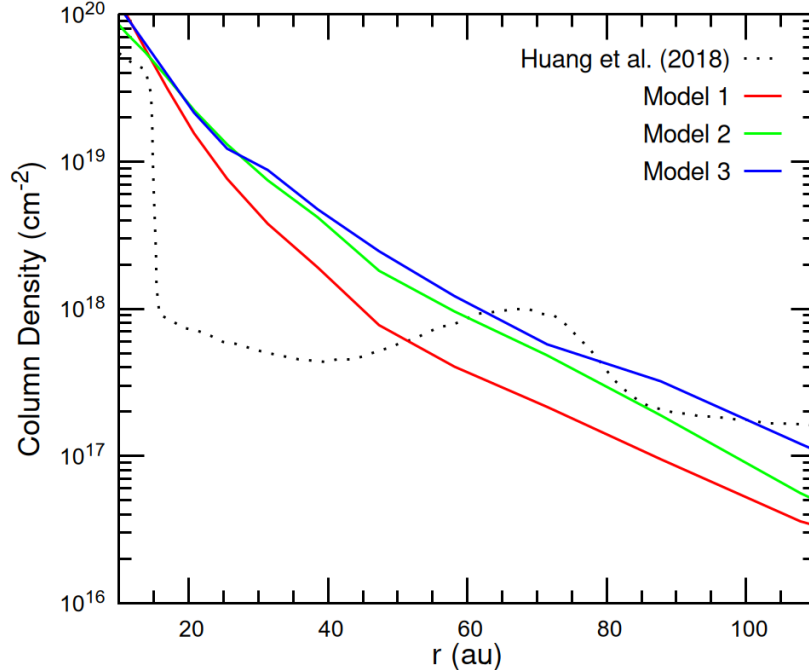


Figure 2: Radial profile of the CO column density for our three models (see Table 1) compared to the ALMA observations of Huang et al.¹⁹

are much larger than 1, in line with Cleaves et al.⁵²

3 Results

The chemistry in each cell of the disk is solved in a time-dependent fashion. Yet, the results presented in this work are steady-state abundances. This simplifying assumption is based on the chemical time scale, ~ 10 Myr, being comparable to the age of the TW Hya system, in the range 7 – 10 Myr.⁵³

The UGAN chemical network being reliable at kinetic temperatures lower than 100 K, our chemical models are limited to the regions of the disk that fulfill this upper limit. In practice, the molecular layer as defined above falls inside this upper limit, except marginally below 90 au in Model 3 (see Fig. 1). Finally, a uniform cosmic-ray (CR) ionization rate was fixed at $\zeta = 5 \times 10^{-19} \text{ s}^{-1}$ ^{14,17} in all models.

According to the temperature structure in our models, the CO snow-line is located at

≈ 15 au, well within the 11-33 au range derived from ALMA observations.^{19,21} In this region, our chemical calculations are not reliable because photodissociation is not included, while the flux from the star (direct and indirect) cannot be neglected.¹⁷ Therefore, we start our calculation at $r = 20$ au, corresponding to the observational peak of ortho- and para-H₂CO column densities.¹¹

3.1 Column Density and OPR of Formaldehyde in TW Hya

The radial distribution of ortho- and para-H₂CO provides a critical benchmark for our spin-resolved chemistry model. Figure 3 compares the predicted column densities by our three different models with the ALMA TW Hya observations.¹¹ We note that all data for the seven detected H₂CO transitions (3 para and 4 ortho) were brought to the same resolution of 0.5" by Terwisscha van Scheltinga et al.¹¹ so that the modeled radial profiles were convolved with a Gaussian kernel of 0.5" HPBW, i.e. 30 au. In doing so, we have artificially extended the value of the H₂CO column density at $r = 20$ au down to $r = 4$ au, and set it to zero for lower radii. We checked that the results are only marginally affected if the column density is set to zero for $r < 20$ au.

Models 1 and 2 reproduce the observed profiles within a factor of 2 between 60 and 150 au, while Model 3 agrees within a factor of 3. The effect of the density tapering is visible in Models 2 and 3 beyond 150 au, while the agreement of Model 1 extends to the outer disk region. The impact of the vertical temperature profile is visible in Model 3 between 60 and 150 au, although the discrepancy remains lower than a factor of three. We note that the nitrogen depletion factor δ_N was set to 1.5 as a compromise to best reproduce the H₂CO column density in all three models. However, no depletion of N ($\delta_N = 0$) cannot be excluded and was indeed found to improve the agreement between observations and Model 3.

Figure 4 shows the predicted radial profiles of the H₂CO ortho-to-para ratio. All three models reproduce the observed ratio lower than 2.5 beyond 90 au, with values decreasing down to 1.9 in Models 1 and 2. This strongly suggests that formaldehyde primarily forms

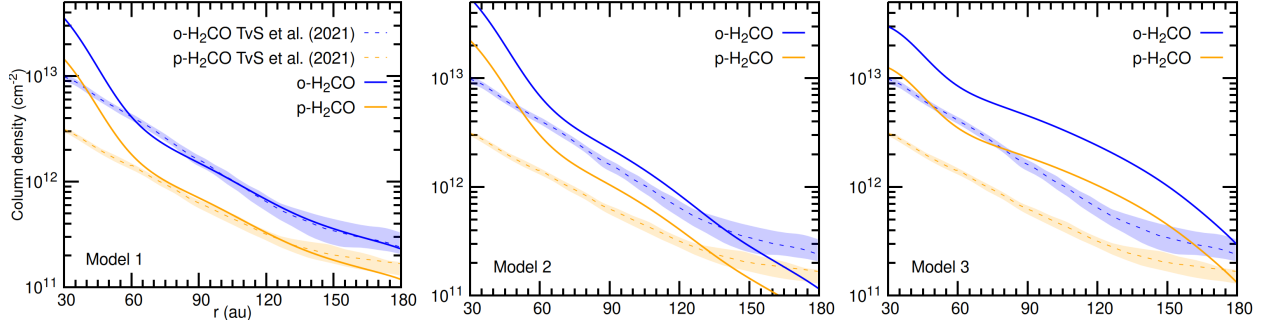


Figure 3: Radial profiles of the column density of ortho- and para- H_2CO (full lines) for the three models (from left to right). In each panel, the shaded areas show the profiles (with 1σ uncertainties) derived from Fig. 6 of Terwisscha van Scheltinga et al.¹¹ via a digital extraction. The computed profiles were convolved with a Gaussian beam of $0.5''$ HPBW (30 au).

in the gas-phase, via the reaction of CH_3 with O (see Section 2.2), in accordance with the nuclear-spin selection rules (derived analytically in the Supporting Information). However, the models predict only weak radial variations of the OPR across the entire disk (beyond 30 au), whereas the observations reveal a strong gradient that rises toward the statistical value of 3 inside ~ 90 au. This discrepancy may indicate that additional processes, such as ice thermal- or photodesorption, are involved, especially if radial drift of icy grains is efficient. Indeed, recent laboratory experiments have shown that the gas-phase OPR of sublimated H_2CO is in the range $\sim 2.9 - 3$, with no correlation with the temperature of the ice,⁴² thus supporting the idea that the observed inner-disk ratios partly reflect ice-related release and mixing processes.

Among the model parameters, density tapering (Model 2 versus Model 1) has little impact on the OPR, while the vertical temperature profile has a noticeable effect on both the OPR value and its radial variation, as evidenced by the differences between models 2 and 3. This result demonstrates that the OPR of H_2CO is a sensitive probe of the kinetic temperature in disks, as expected from its dependence on the OPR of H_2 (see Fig. S2 in Supporting Information), provided that the uncertainties in the derived ortho- and para- H_2CO column densities are sufficiently small ($\sim 10\%$).

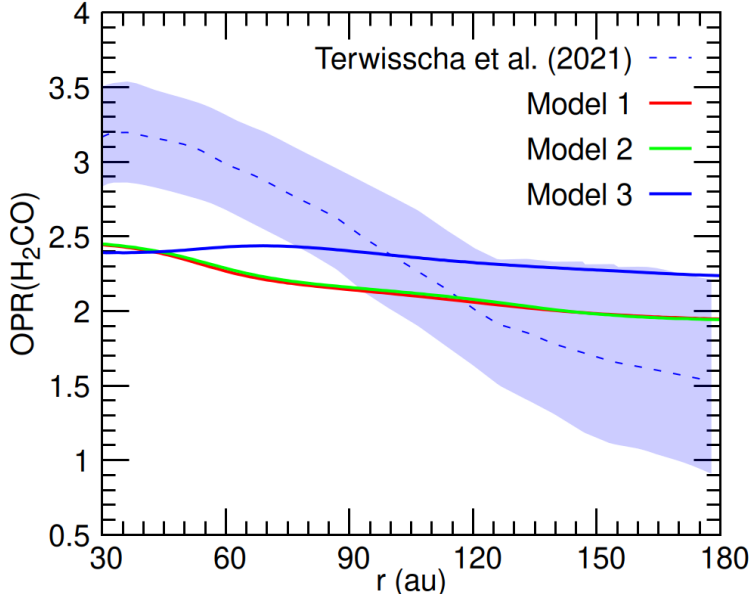


Figure 4: Radial profile of the H_2CO OPR for the three models. Our results are shown with full lines and the shaded areas show the OPR (with 1σ uncertainties) derived from ALMA observations.¹¹

3.2 Effects of the C/O Ratio and the CR Ionization Rate

Finally, we investigate the impact of the $[\text{C}/\text{O}]_{\text{elem}}$ ratio and of ζ on the abundance and OPR of H_2CO for typical physical conditions in the disk ($T_{\text{gas}} = 30$ K and $n_{\text{H}} = 10^8 \text{ cm}^{-3}$, see Fig. 5).

The abundance of H_2CO is strongly affected by the gas-phase $[\text{C}/\text{O}]_{\text{elem}}$ ratio. When $[\text{C}/\text{O}]_{\text{elem}} \lesssim 1$, sufficient atomic oxygen remains available for the reaction $\text{CH}_3 + \text{O} \longrightarrow \text{H}_2\text{CO} + \text{H}$, and H_2CO forms efficiently. In contrast, when $[\text{C}/\text{O}]_{\text{elem}} \gtrsim 1$, most of the oxygen becomes locked in CO, leaving very little free atomic O in the gas. Despite the concomitant increase of the CH_3 abundance in this regime, the abundance of H_2CO drops significantly, by up to three orders of magnitude, due to the enhancement of the abundance of C_2H and CN radicals, which become important H_2CO destroyers.

The impact of the cosmic-ray ionization rate is qualitatively different. The abundances of HCO^+ and CH_3 , respectively destruction and formation partners of H_2CO , both increase with ζ , and the net result is an increase of the H_2CO abundance. Actually, at $[\text{C}/\text{O}]_{\text{elem}} = 1$,

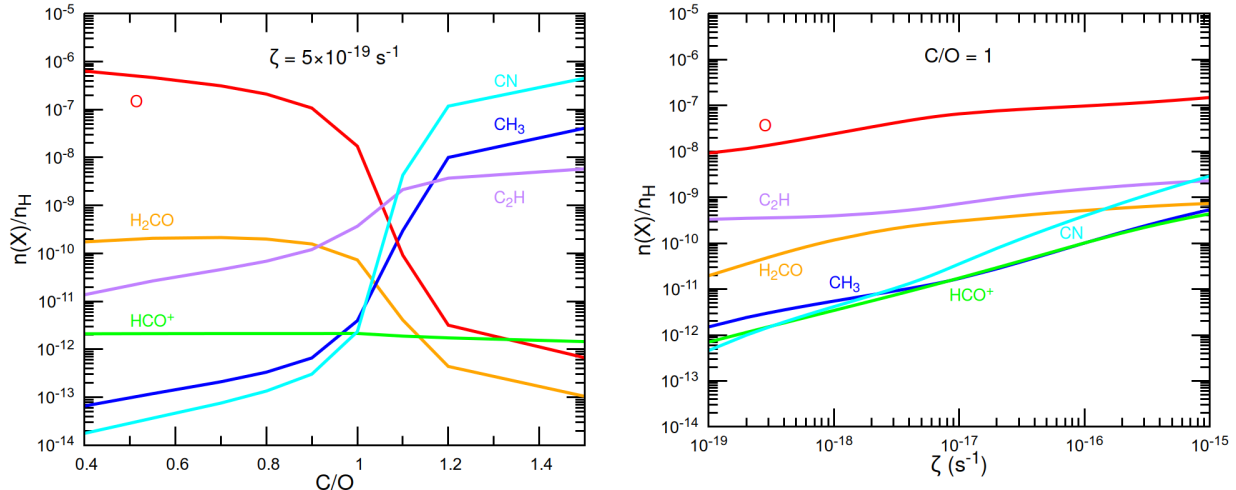


Figure 5: Steady-state abundances of the main precursors and sinks of H_2CO , as a function of $[\text{C}/\text{O}]_{\text{elem}}$, for $\zeta = 5 \times 10^{-19} \text{ s}^{-1}$ (left) and as a function of ζ for $[\text{C}/\text{O}]_{\text{elem}} = 1$ (right). Abundances are computed for a typical cell of the disk models, i.e., $T_{\text{gas}} = 30\text{K}$ and $n_{\text{H}} = 10^8 \text{ cm}^{-3}$.

the destruction of H_2CO is dominated by C_2H .

These results emphasize that the gas-phase abundance of H_2CO is highly sensitive to both the $[\text{C}/\text{O}]_{\text{elem}}$ ratio and the cosmic-ray ionization rate. Observations of H_2CO in multiple disks (where other relevant tracers are detected) could therefore provide valuable constraints on these fundamental but otherwise elusive parameters.

Conversely, the OPR of H_2CO is found to be largely unaffected by these two parameters (over the investigated ranges), with variations of less than 10%. This reflects the fact that the OPR of H_2CO is mostly controlled by the OPR of H_2 , which in turn depends primarily on the kinetic temperature above 15 K (see Supporting Information).

4 Conclusions and Perspectives

We have presented the first study of the nuclear-spin-resolved chemistry of formaldehyde in disks, focusing on the transition disk TW Hya. The self-consistent description of nuclear spin states of carbon, nitrogen, oxygen and sulfur hydrides of the UGAN network allows us to compute the spatial distribution of ortho- and para- H_2CO in a model of TW Hya that

reproduces the CO column density and includes a three-layer disk model (photodissociation, molecular, and freeze-out). Photodissociation by stellar UV and X-ray is not included and the present models focus on the gas-phase chemistry of H₂CO in the molecular layer. The present physicochemical disk model reproduces the observed radial profile of the ortho- and para-H₂CO column density to within a factor of two from 60 to 150 au. The derived ortho-to-para ratio of H₂CO is also well reproduced, especially the values lower than the statistical ratio of 3 measured in this disk. In contrast with the observations, our model predicts a relatively constant radial profile, with a ratio of $\sim 1.9 - 2.5$, which is lower than observed at radii below 70 au. It is found that the vertical temperature profile has a noticeable effect on the OPR of H₂CO. However, the uncertainties in the observed OPR value and radial profile are currently too large to make this OPR a sensitive probe of the vertical temperature profile. Future observations including more transitions of H₂CO would be highly valuable. The discrepancy between the predicted and measured OPR at radii below 70 au suggests that processes such as desorption combined with vertical/radial mixing could be important in this region, leading to higher values of the OPR than obtained by our present model. The total abundance of H₂CO is also found to be highly sensitive to the elemental ratio $[C/O]_{\text{elem}}$ in the gas-phase, decreasing by three orders of magnitude at $C/O > 1.2$. Similarly, the cosmic-ray ionization rate also has a strong impact on the abundance of H₂CO. Observations of H₂CO in a sample of disks would provide an observational test of the dependence of its abundance on $[C/O]_{\text{elem}}$ and ζ .

Supporting Information Available

- Figure S1. Details of the temperature and density profiles.
- Figure S2. Analytical ortho-to-para ratio of H₂CO.

Acknowledgement

We thank the anonymous reviewers for their careful reading and valuable comments. The authors acknowledge the financial support of the University Grenoble Alpes for funding Hideko Nomura as a Visiting Professor. This research was also supported by the International Space Science Institute (ISSI) in Bern, through ISSI International Team project “Understanding Nuclear Spin Temperatures in Astronomical Environments ISSI Team 25-648”. RLG also thanks the financial support from the French Agence Nationale de la Recherche (ANR) through the project MAPSAJE (ANR-24-CE31-2126-01).

References

- (1) Henning, T.; Semenov, D. Chemistry in Protoplanetary Disks. *Chem. Rev.* **2013**, *113*, 9016–9042.
- (2) Öberg, K. I.; Facchini, S.; Anderson, D. E. Protoplanetary Disk Chemistry. *Annu. Rev. Astron. Astrophys.* **2023**, *61*, 287–328.
- (3) Mumma, M. J.; Charnley, S. B. The Chemical Composition of Comets—Emerging Taxonomies and Natal Heritage. *Annu. Rev. Astron. Astrophys.* **2011**, *49*, 471–524.
- (4) Hama, T.; Kouchi, A.; Watanabe, N. The Ortho-to-para Ratio of Water Molecules Desorbed from Ice Made from Para-water Monomers at 11 K. *Astrophys. J. Lett.* **2018**, *857*, L13.
- (5) Faure, A.; Hily-Blant, P.; Rist, C.; Pineau des Forêts, G.; Matthews, A.; Flower, D. R. The ortho-to-para ratio of water in interstellar clouds. *Mon. Not. R. Astron. Soc.* **2019**, *487*, 3392–3403.
- (6) Rist, C.; Faure, A.; Hily-Blant, P.; Le Gal, R. Nuclear-Spin Selection Rules in the Chemistry of Interstellar Nitrogen Hydrides. *J. Phys. Chem. A* **2013**, *117*, 9800–9806.

- (7) Faure, A.; Hily-Blant, P.; Le Gal, R.; Rist, C.; Pineau des Forêts, G. Ortho-Para Selection Rules in the Gas-phase Chemistry of Interstellar Ammonia. *Astrophys. J.* **2013**, *770*, L2.
- (8) Le Gal, R.; Hily-Blant, P.; Faure, A.; Pineau des Forêts, G.; Rist, C.; Maret, S. Interstellar chemistry of nitrogen hydrides in dark clouds. *Astron. Astrophys.* **2014**, *562*, A83.
- (9) Hily-Blant, P.; Faure, A.; Rist, C.; Pineau des Forêts, G.; Flower, D. R. Modelling the molecular composition and nuclear-spin chemistry of collapsing pre-stellar sources. *Mon. Not. R. Astron. Soc.* **2018**, *477*, 4454–4472.
- (10) Guzmán, V. V.; Öberg, K. I.; Carpenter, J.; Le Gal, R.; Qi, C.; Pagues, J. H₂CO Ortho-to-para Ratio in the Protoplanetary Disk HD 163296. *Astrophys. J.* **2018**, *864*, 170.
- (11) Terwisscha van Scheltinga, J. et al. The TW Hya Rosetta Stone Project. II. Spatially Resolved Emission of Formaldehyde Hints at Low-temperature Gas-phase Formation. *Astrophys. J.* **2021**, *906*, 111.
- (12) Andrews, S. M.; Wilner, D. J.; Hughes, A. M.; Qi, C.; Rosenfeld, K. A.; Öberg, K. I.; Birnstiel, T.; Espaillat, C.; Cieza, L. A.; Williams, J. P.; Lin, S.-Y.; Ho, P. T. P. The TW Hya disk at 870mic: comparison of CO and dust radial structures. *Astrophys. J.* **2011**, *744*, 162.
- (13) Rosenfeld, K. A.; Andrews, S. M.; Wilner, D. J.; Kastner, J. H.; McClure, M. K. The structure of the evolved circumbinary disk around V4046 Sgr. *Astrophys. J.* **2013**, *775*, 136.
- (14) Cleeves, L. I.; Bergin, E. A.; Qi, C.; Adams, F. C.; Öberg, K. I. Constraining the x-ray and cosmic-ray ionization chemistry of the TW Hya protoplanetary disk: evidence for a sub-interstellar cosmic-ray rate. *Astrophys. J.* **2015**, *799*, 204.

- (15) Le Gal, R.; Öberg, K. I.; Loomis, R. A.; Pegues, J.; Bergner, J. B. Sulfur Chemistry in Protoplanetary Disks: CS and H₂CS. *Astrophys. J.* **2019**, *876*, 72.
- (16) Lee, S.; Nomura, H.; Furuya, K.; Lee, J.-E. Modeling Nitrogen Fractionation in the Protoplanetary Disk around TW Hya: Model Constraints on Grain Population and Carbon-to-oxygen Elemental Abundance Ratio. *Astrophys. J.* **2021**, *908*, 82.
- (17) Lee, S.; Nomura, H.; Furuya, K. Carbon Isotope Chemistry in Protoplanetary Disks: Effects of C/O Ratios. *Astrophys. J.* **2024**, *969*, 41.
- (18) Dartois, E.; Dutrey, A.; Guilloteau, S. Structure of the DM Tau Outer Disk: Probing the vertical kinetic temperature gradient. *Astron. Astrophys.* **2003**, *399*, 773–787.
- (19) Huang, J.; Andrews, S. M.; Cleaves, L. I.; Öberg, K. I.; Wilner, D. J.; Bai, X.; Birnstiel, T.; Carpenter, J.; Hughes, A. M.; Isella, A.; Pérez, L. M.; Ricci, L.; Zhu, Z. CO and Dust Properties in the TW Hya Disk from High-resolution ALMA Observations. *Astrophys. J.* **2018**, *852*, 122.
- (20) Canta, A.; Teague, R.; Gal, R. L.; Öberg, K. I. The First Detection of CH₂CN in a Protoplanetary Disk. *Astrophys. J.* **2021**, *922*, 62.
- (21) Qi, C.; Öberg, K. I.; Wilner, D. J.; D'Alessio, P.; Bergin, E.; Andrews, S. M.; Blake, G. A.; Hogerheijde, M. R.; van Dishoeck, E. F. Imaging of the CO Snow Line in a Solar Nebula Analog. *Science* **2013**, *341*, 630–632.
- (22) Kama, M.; Bruderer, S.; van Dishoeck, E. F.; Hogerheijde, M.; Folsom, C. P.; Miotello, A.; Fedele, D.; Belloche, A.; Güsten, R.; Wyrowski, F. Volatile-carbon locking and release in protoplanetary disks - A study of TW Hya and HD 100546. *Astron. Astrophys.* **2016**, *592*, A83.
- (23) Wagenblast, R.; Hartquist, T. W. Non-equilibrium level populations of molecular hydrogen -II. Models of ZET OPH cloud. *Mon. Not. R. Astron. Soc.* **1989**, *237*, 1019–1025.

- (24) Flower, D. R.; Pineau Des Forêts, G.; Walmsley, C. M. The abundances of nitrogen-containing molecules during pre-protostellar collapse. *Astron. Astrophys.* **2006**, *456*, 215–223.
- (25) Oka, T. Nuclear spin selection rules in chemical reactions by angular momentum algebra. *Journal of Molecular Spectroscopy* **2004**, *228*, 635–639.
- (26) Quack, M. Detailed symmetry selection rules for reactive collisions. *Mol. Phys.* **1977**, *34*, 477–504.
- (27) Hu, M.-G.; Liu, Y.; Nichols, M. A.; Zhu, L.; Quéméner, G.; Dulieu, O.; Ni, K.-K. Nuclear spin conservation enables state-to-state control of ultracold molecular reactions. *Nat. Chem.* **2021**, *13*, 435–440.
- (28) Jiménez-Redondo, M.; Sipilä, O.; Dahl, R.; Caselli, P.; Jusko, P. Cl⁺ and HCl⁺ in Reaction with H₂ and Isotopologues: A Glance into H Abstraction and Indirect Exchange at Astrophysical Conditions. *ACS Earth and Space Chem.* **2025**, *9*, 782–788.
- (29) Le Gal, R.; Xie, C.; Herbst, E.; Talbi, D.; Guo, H.; Muller, S. The ortho-to-para ratio of H₂Cl⁺: Quasi-classical trajectory calculations and new simulations in light of new observations. *Astron. Astrophys.* **2017**, *608*, A96.
- (30) Harju, J.; Caselli, P.; Sipilä, O.; Spezzano, S.; Belloche, A.; Bizzocchi, L.; Pineda, J. E.; Redaelli, E.; Wyrowski, F. Statistical nuclear spin ratios of deuterated ammonia in the pre-stellar core L1544. *Astron. Astrophys.* **2025**, *700*, A141.
- (31) Hily-Blant, P.; Pineau des Forêts, G.; Faure, A.; Flower, D. R. Depletion and fractionation of nitrogen in collapsing cores. *Astron. Astrophys.* **2020**, *643*, A76.
- (32) Hily-Blant, P.; Pineau des Forêts, G.; Faure, A.; Lique, F. Sulfur gas-phase abundance in dense cores. *Astron. Astrophys.* **2022**, *658*, A168.

- (33) Kamińska, M.; Zhaunerchyk, V.; Vigren, E.; Danielsson, M.; Hamberg, M.; Geppert, W. D.; Larsson, M.; Rosén, S.; Thomas, R. D.; Semaniak, J. Dissociative recombination of CH_5^+ and CD_5^+ : Measurement of the product branching fractions and the absolute cross sections, and the breakup dynamics in the $\text{CH}_3+\text{H}+\text{H}$ product channel. *Phys. Rev. A* **2010**, *81*, 062701.
- (34) West, N. A.; Li, L. H. D.; Millar, T. J.; Van de Sande, M.; Rutter, E.; Blitz, M. A.; Lehman, J. H.; Decin, L.; Heard, D. E. Experimental and theoretical study of the low-temperature kinetics of the reaction of CN with CH_2O and implications for interstellar environments. *Phys. Chem. Chem. Phys.* **2023**, *25*, 7719–7733.
- (35) Douglas, K. M.; West, N. A.; Lucas, D. I.; Van de Sande, M.; Blitz, M. A.; Heard, D. E. Experimental and Theoretical Investigation of the Reaction of C_2H with Formaldehyde (CH_2O) at Very Low Temperatures and Application to Astrochemical Models. *ACS Earth Space Chem.* **2024**, *8*, 2428–2441.
- (36) Hamberg, M.; Geppert, W. D.; Thomas, R. D.; Zhaunerchyk, V.; Österdahl, F.; Ehlerding, A.; Kaminska, M.; Semaniak, J.; Ugglas, M. A.; Källberg, A.; Paal, A.; Simonsson, A.; Larsson, M. Experimental determination of dissociative recombination reaction pathways and absolute reaction cross-sections of CH_2OH^+ , CD_2OD^+ and CD_2 . *Molecular Physics* **2007**, *105*, 899–906.
- (37) Bacmann, A.; García-García, E.; Faure, A. Detection of protonated formaldehyde in the prestellar core L1689B. *Astron. Astrophys.* **2016**, *588*, L8.
- (38) Klemperer, W. Astronomical Chemistry. *Annu. Rev. Phys. Chem.* **2011**, *62*, 173–184.
- (39) Watanabe, N.; Kouchi, A. Efficient Formation of Formaldehyde and Methanol by the Addition of Hydrogen Atoms to CO in H_2O -CO Ice at 10 K. *Astrophys. J. Lett.* **2002**, *571*, L173–L176.

- (40) Faure, M.; Bacmann, A.; Faure, A.; Quirico, E.; Boduch, P.; Domaracka, A.; Rothard, H. Cosmic-ray induced sputtering of interstellar formaldehyde ices. *Astron. Astrophys.* **2025**, *693*, A30.
- (41) Boogert, A. C. A.; Gerakines, P. A.; Whittet, D. C. B. Observations of the icy universe. *Annu. Rev. Astron. Astrophys.* **2015**, *53*, 541–581.
- (42) Yocum, K. M.; Wilkins, O. H.; Bardwell, J. C.; Milam, S. N.; Gerakines, P. A. Gas-phase Ortho-to-para Ratio of Formaldehyde Formed at Low Temperatures in Laboratory Ices. *Astrophys. J. Lett.* **2023**, *958*, L41.
- (43) Gerlich, D. Probing the structure of CH₅⁺ ions and deuterated variants via collisions. *Phys. Chem. Chem. Phys.* **2005**, *7*, 1583.
- (44) Hillenbrand, P.-M.; de Ruelle, N.; Urbain, X.; Savin, D. W. Branching Ratio for O + H₃⁺ Forming OH⁺ + H₂ and H₂O⁺ + H. *Astrophys. J.* **2022**, *927*, 47.
- (45) Hack, W.; Hold, M.; Hoyermann, K.; Wehmeyer, J.; Zeuch, T. Mechanism and rate of the reaction CH₃ + O—revisited. *Phys. Chem. Chem. Phys.* **2005**, *7*, 1977–1984.
- (46) Xu, Z. F.; Raghunath, P.; Lin, M. C. Ab Initio Chemical Kinetics for the CH₃ + O(3P) Reaction and Related Isomerization–Decomposition of CH₃O and CH₂OH Radicals. *J. Phys. Chem. A* **2015**, *119*, 7404–7417, PMID: 25751420.
- (47) Heard, D. E. Rapid Acceleration of Hydrogen Atom Abstraction Reactions of OH at Very Low Temperatures through Weakly Bound Complexes and Tunneling. *Acc. Chem. Res.* **2018**, *51*, 2620–2627.
- (48) Su, T.; Chesnavich, W. J. Parametrization of the ion-polar molecule collision rate constant by trajectory calculations. *J. Chem. Phys.* **1982**, *76*, 5183–5185.
- (49) Wakelam, V.; Gratier, P.; Loison, J.-C.; Hickson, K. M.; Penguen, J.; Mechineau, A. The 2024 KIDA network for interstellar chemistry. *Astron. Astrophys.* **2024**, *689*, A63.

- (50) Le Gal, R.; Brady, M. T.; Öberg, K. I.; Roueff, E.; Le Petit, F. The Role of C/O in Nitrile Astrochemistry in PDRs and Planet-forming Disks. *Astrophys. J.* **2019**, *886*, 86.
- (51) Qi, C.; Wilner, D. J. Evidence for a Sharp CO Snow Line Transition in a Protoplanetary Disk and Implications for Millimeter-wave Observations of CO Isotopologues. *Astrophys. J.* **2024**, *977*, 60.
- (52) Cleeves, L.; Öberg, K. I.; Wilner, D. J.; Huang, J.; Loomis, R. A.; Andrews, S. M.; Guzman, V. V. Constraining Gas-phase Carbon, Oxygen, and Nitrogen in the IM Lup Protoplanetary Disk. *Astrophys. J.* **2018**, *865*, 155.
- (53) Ruane, G.; Mawet, D.; Kastner, J.; Meshkat, T.; Bottom, M.; Femenía Castellá, B.; Absil, O.; Gomez Gonzalez, C.; Huby, E.; Zhu, Z.; Jensen-Clem, R.; Choquet, É.; Serabyn, E. Deep Imaging Search for Planets Forming in the TW Hya Protoplanetary Disk with the Keck/NIRC2 Vortex Coronagraph. *Astron. J.* **2017**, *154*, 73.

Supporting Information:

Ortho-Para Chemistry of H₂CO in the Protoplanetary Disk TW Hya

M. Gaillard,[†] A. Faure,[†] P. Hily-Blant,[†] R. Le Gal,^{*,†,‡} S. Lee,[¶] H. Nomura,^{§,||} and
K. Furuya^{⊥,#}

[†]*Université Grenoble Alpes, CNRS, IPAG, F-38000 Grenoble, France*

[‡]*IRAM, 300 rue de la piscine, F-38406 Saint-Martin d'Hères, France*

[¶]*Korea Astronomy and Space Science Institute, 776 Daedeok-daero, Yuseong-gu, Daejeon
34055, Republic of Korea*

[§]*National Astronomical Observatory of Japan, 2-21-1 Osawa, Mitaka, Tokyo 181-8588,
Japan*

^{||}*Department of Astronomical Science, The Graduate University for Advanced Studies,
SOKENDAI, 2-21-1 Osawa, Mitaka, Tokyo, 181-8588, Japan*

[⊥]*RIKEN Pioneering Research Institute, 2-1 Hirosawa, Wako-shi, Saitama, 351-0198,
Japan*

[#]*Department of Astronomy, Graduate School of Science, The University of Tokyo, Tokyo,
113-0033, Japan*

E-mail: romane.le-gal@univ-grenoble-alpes.fr

Physical structure of the disk models

Figure S1 shows the vertical temperature and density profiles in the three models used in this work, and are compared to the model of Lee et al.^{S1} which is taken as a reference.

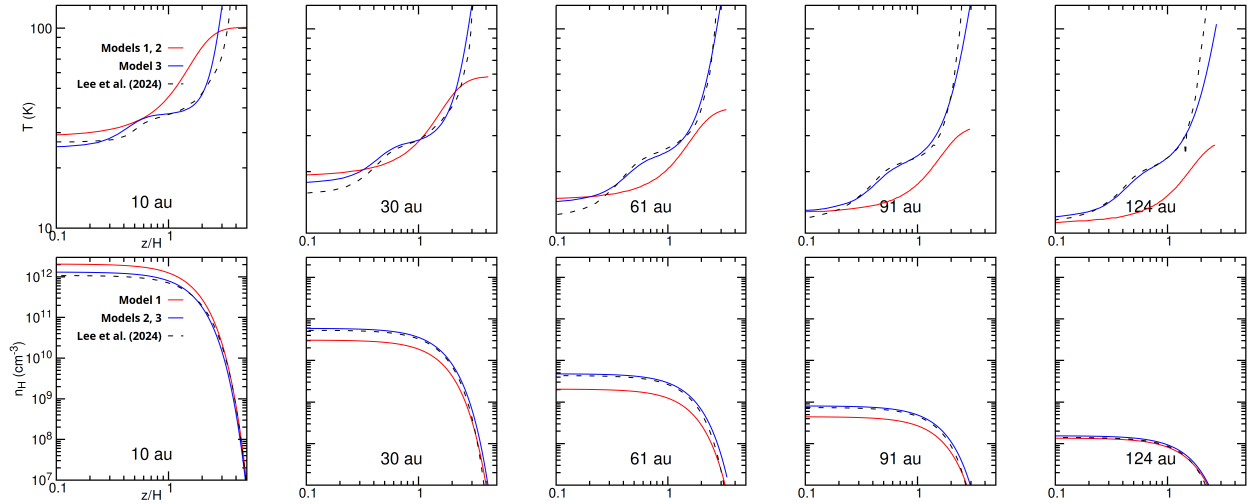


Figure S1: Comparison of the three parametric models (see Table 2 of the main paper) for the gas temperature (top) and H nuclei density (bottom). The vertical profiles are shown as function of z/H for several representative radii indicated in each panel.

Analytical ortho-to-para ratio of H_2CO

We derive below the analytical ortho-to-para ratio (OPR) of formaldehyde following its formation via the reaction of CH_3 with $\text{O}(^3P)$ atoms. Since the nuclear-spin thermalization of CH_3^+ by H_2 collisions should drive the OPR of CH_3^+ toward thermal equilibrium above a critical temperature $T_{\text{crit}} \sim 15 - 20$ K (see Ref. 1), we will assume $\text{OPR}(\text{CH}_3^+) = 1$ in the following.

Nuclear-spin branching ratios for the slow radiative association between CH_3^+ and H_2

can be derived using the approach of Quack^{S2}:

$$\text{pCH}_3^+ + \text{pH}_2 \rightarrow \begin{cases} \text{pCH}_5^+ + h\nu & 0 \\ \text{mCH}_5^+ + h\nu & 1 \\ \text{oCH}_5^+ + h\nu & 0 \end{cases} \quad (1)$$

$$\text{pCH}_3^+ + \text{oH}_2 \rightarrow \begin{cases} \text{pCH}_5^+ + h\nu & 0 \\ \text{mCH}_5^+ + h\nu & \frac{1}{3} \\ \text{oCH}_5^+ + h\nu & \frac{2}{3} \end{cases} \quad (2)$$

$$\text{oCH}_3^+ + \text{pH}_2 \rightarrow \begin{cases} \text{pCH}_5^+ + h\nu & 0 \\ \text{mCH}_5^+ + h\nu & 0 \\ \text{oCH}_5^+ + h\nu & 1 \end{cases} \quad (3)$$

$$\text{oCH}_3^+ + \text{oH}_2 \rightarrow \begin{cases} \text{pCH}_5^+ + h\nu & \frac{1}{2} \\ \text{mCH}_5^+ + h\nu & \frac{1}{6} \\ \text{oCH}_5^+ + h\nu & \frac{1}{3} \end{cases} \quad (4)$$

From the above equations, we derive the OPR, meta-to-para ratio (MPR) and ortho-to-meta ratio (OMR) of CH_5^+ :

$$\text{OPR}(\text{CH}_5^+) = \frac{2\text{OPR}(\text{H}_2) + 2}{\text{OPR}(\text{H}_2)} \quad (5)$$

$$\text{MPR}(\text{CH}_5^+) = \frac{2 + \text{OPR}(\text{H}_2)}{\text{OPR}(\text{H}_2)} \quad (6)$$

$$\text{OMR}(\text{CH}_5^+) = \frac{2\text{OPR}(\text{H}_2) + 2}{2 + \text{OPR}(\text{H}_2)} \quad (7)$$

Now, by combining the above equations with the nuclear-spin branching ratio for the DR of

CH_5^+ :

$$\text{pCH}_5^+ + \text{e}^- \rightarrow \begin{cases} \text{pCH}_3 + \text{pH}_2 & 0 \\ \text{pCH}_3 + \text{oH}_2 & 0 \\ \text{oCH}_3 + \text{pH}_2 & 0 \\ \text{oCH}_3 + \text{oH}_2 & 1 \end{cases} \quad (8)$$

$$\text{mCH}_5^+ + \text{e}^- \rightarrow \begin{cases} \text{pCH}_3 + \text{pH}_2 & \frac{2}{5} \\ \text{pCH}_3 + \text{oH}_2 & \frac{2}{5} \\ \text{oCH}_3 + \text{pH}_2 & 0 \\ \text{oCH}_3 + \text{oH}_2 & \frac{1}{5} \end{cases} \quad (9)$$

$$\text{oCH}_5^+ + \text{e}^- \rightarrow \begin{cases} \text{pCH}_3 + \text{pH}_2 & 0 \\ \text{pCH}_3 + \text{oH}_2 & \frac{1}{2} \\ \text{oCH}_3 + \text{pH}_2 & \frac{1}{4} \\ \text{oCH}_3 + \text{oH}_2 & \frac{1}{4} \end{cases} \quad (10)$$

we obtain:

$$\text{OPR}(\text{CH}_3) = \frac{7 + 11\text{OPR}(\text{H}_2)}{13 + 9\text{OPR}(\text{H}_2)} \quad (11)$$

By combining Eq. 11 with the branching ratio for the formation of H_2CO :

$$\text{pCH}_3 + \text{O} \rightarrow \begin{cases} \text{pH}_2\text{CO} + \text{H} & \frac{1}{2} \\ \text{oH}_2\text{CO} + \text{H} & \frac{1}{2} \end{cases} \quad (12)$$

$$\text{oCH}_3 + \text{O} \rightarrow \begin{cases} \text{pH}_2\text{CO} + \text{H} & 0 \\ \text{oH}_2\text{CO} + \text{H} & 1 \end{cases} \quad (13)$$

we finally obtain:

$$\text{OPR}(\text{H}_2\text{CO}) = 1 + 2\text{OPR}(\text{CH}_3) = \frac{27 + 31\text{OPR}(\text{H}_2)}{13 + 9\text{OPR}(\text{H}_2)} \quad (14)$$

We note that if $\text{OPR}(\text{H}_2)=3$, the above equations predict that $\text{OPR}(\text{CH}_3)=1$ and $\text{OPR}(\text{H}_2\text{CO})=3$, as expected in the statistical limit. On the other hand, in a *para*-rich H_2 gas ($\text{OPR}(\text{H}_2)\ll 1$), we predict $\text{OPR}(\text{CH}_3)=7/13 \sim 0.54$ and $\text{OPR}(\text{H}_2\text{CO})=27/13 \sim 2.1$.

OPRs of H_2 , CH_3 and H_2CO

As an application of the above analytical treatment, we show in Fig. S2, the OPRs of H_2 , CH_3 and H_2CO as function of kinetic temperature for typical density and ionization conditions in the TW Hya protoplanetary disk: $n_{\text{H}} = 10^8 \text{cm}^{-3}$ and $\zeta = 5 \times 10^{-19} \text{s}^{-1}$, and with the fixed depletion factors $\delta_{\text{C}} = 30$ and $\delta_{\text{N}} = 1.5$. The chemistry was first solved at steady-state with the UGAN network for kinetic temperatures in the range 5 – 50 K and the above density and ionization rate. Equations (11) and (14) were then employed to compute the analytical OPRs of CH_3 and H_2CO , respectively, as function of the UGAN OPR of H_2 plotted in Fig. 1 (left panel). We can first observe that $\text{OPR}(\text{H}_2)$ is suprathermal below ~ 15 K and closely follows thermal equilibrium at higher temperatures, as expected (see Faure et al.^{S3}). In contrast, the UGAN OPRs of CH_3 and H_2CO deviate significantly from thermal values, with a relatively weak temperature dependence. In particular, the OPR of H_2CO never goes below 1.8, is suprathermal below 11 K, and increases towards the statistical value beyond 50 K. The good agreement between the UGAN results and the analytic calculations clearly demonstrates that the OPR of H_2CO is governed by the OPR of H_2 , via the formation of CH_5^+ (Eqs. 1-4) and CH_3 (Eqs. 8-10). We note, however, that the analytical OPRs slightly departs from the UGAN values. This can be explained by the actual temperature dependence of the OPR of CH_3^+ , which drops below unity at temperatures lower than ~ 25 K, and also by the secondary formation reactions of CH_5^+ and H_2CO via $\text{CH}_4 + \text{H}_3^+$ and $\text{H}_2\text{COH}^+ + \text{e}^-$, respectively, which are neglected in our analytical treatment.

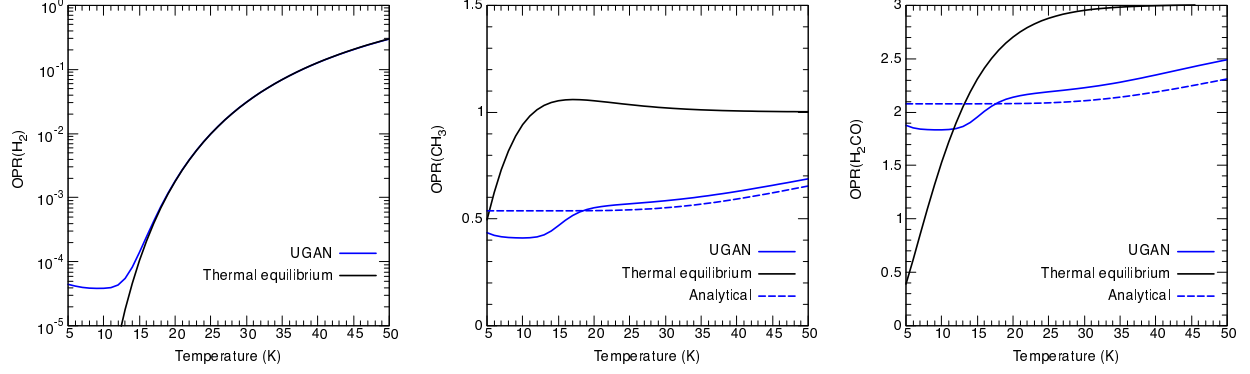


Figure S2: OPRs of H_2 , CH_3 and H_2CO as function of kinetic temperature for $n_{\text{H}} = 10^8 \text{cm}^{-3}$ and $\zeta = 5 \times 10^{-19} \text{s}^{-1}$, with depletion factors $\delta_{\text{C}} = 30$ and $\delta_{\text{N}} = 1.5$. The UGAN results are compared to thermal equilibrium and, except for H_2 , to the analytical model. See text for details.

References

- (S1) Lee, S.; Nomura, H.; Furuya, K. Carbon Isotope Chemistry in Protoplanetary Disks: Effects of C/O Ratios. *Astrophys. J.* **2024**, *969*, 41.
- (S2) Quack, M. Detailed symmetry selection rules for reactive collisions. *Mol. Phys.* **1977**, *34*, 477–504.
- (S3) Faure, A.; Hily-Blant, P.; Le Gal, R.; Rist, C.; Pineau des Forêts, G. Ortho-Para Selection Rules in the Gas-phase Chemistry of Interstellar Ammonia. *Astrophys. J.* **2013**, *770*, L2.